Title

An accurate and efficient laser-envelope solver for the modeling of laser-plasma accelerators

Journal

Plasma Physics and Controlled Fusion, 60(1)

ISSN

0741-3335

Authors

Benedetti, C
Schroeder, CB
Geddes, CGR
et al.

Publication Date

2018

DOI

10.1088/1361-6587/aa8977

Peer reviewed

An accurate and efficient laser-envelope solver for the modeling of laser-plasma accelerators

C Benedetti
Lawrence Berkeley National Laboratory, Berkeley, California 94720, USA

C B Schroeder
Lawrence Berkeley National Laboratory, Berkeley, California 94720, USA

C G R Geddes
Lawrence Berkeley National Laboratory, Berkeley, California 94720, USA

E Esarey
Lawrence Berkeley National Laboratory, Berkeley, California 94720, USA

W P Leemans
Lawrence Berkeley National Laboratory, Berkeley, California 94720, USA

Abstract. Detailed and reliable numerical modeling of laser-plasma accelerators, where a short and intense laser pulse interacts with an underdense plasma over distances of up to a meter, is a formidably challenging task. This is due to the great disparity among the length scales involved in the modeling, ranging from the micron scale of the laser wavelength to the meter scale of the total laser-plasma interaction length. The use of the time-averaged ponderomotive force approximation, where the laser pulse is described by means of its envelope, enables efficient modeling of laser-plasma accelerators by removing the need to model the details of electron motion at the laser wavelength scale. Furthermore, it allows simulations in cylindrical geometry which captures relevant 3D physics at 2D computational cost. A key element of any code based on the time-averaged ponderomotive force approximation is the laser envelope solver. In this paper we present the accurate and efficient envelope solver used in the code INF&RNO (INtegrated Fluid & paRticle simulatioN cOde). The features of the INF&RNO laser solver enable an accurate description of the laser pulse evolution deep into depletion even at a reasonably low resolution, resulting in significant computational speed-ups.

1. Introduction

Laser-plasma accelerators (LPAs) have received substantial theoretical and experimental interest because of their ability to produce large accelerating gradients, enabling compact accelerating structures [1]. In an LPA, a short and intense laser pulse propagating in an underdense plasma ponderomotively drives a plasma wave (or wakefield). The plasma wave has a relativistic phase velocity (of the order of the driver velocity),

and can support large longitudinal and transverse fields suitable for accelerating and focusing a particle bunch properly delayed with respect to the laser driver. For optimal wake excitation the laser pulse length, L, has to be $\sim k_p^{-1}$ [where $k_p = \omega_p/c$ is the plasma skin depth, $\omega_p = (4\pi n_0 e^2/m)^{1/2}$ is the plasma frequency for a plasma with a density n_0, m and e being, respectively, the electron mass and charge, and c is the speed of light], and the laser intensity has to be high enough so that the peak normalized laser field strength satisfies $a_0 = eA_0/mc^2 \simeq 8.5\cdot 10^{-10}\lambda_0[\mu\text{m}](I_0[\text{W/cm}^2])^{1/2} \sim 1$ (where A_0 is the peak amplitude of the laser vector potential, λ_0 the laser wavelength, typically ~ 1 μm , and I_0 the laser peak intensity). The accelerating gradient in an LPA driven by an optimal laser pulse and operating at a density n_0 is of order $E_z \sim E_0 = mc\omega_p/e \propto n_0^{1/2}$ (for $n_0 \sim 10^{18}$ cm^{-3}, $E_0 \simeq 100$ GV/m, which is three orders of magnitude higher than in conventional radio-frequency-based accelerators). The acceleration length, L_{acc}, is limited by laser driver depletion or bunch dephasing (i.e., the accelerating particles outrun the wake), and scales with the density as $L_{\text{acc}} \propto n_0^{-3/2}$ (for $n_0 \sim 10^{18}$ cm^{-3}, L_{acc} is $\sim$ cm-scale). The energy gain provided by an LPA stage is then $\Delta W \propto E_z \times L_{\text{acc}} \propto n_0^{-1}$. For instance, a mm-scale LPA with $n_0 \simeq 10^{19}$ cm^{-3} has produced in experiments ~ 100 MeV electron beams [2, 3, 4], while a few cm-long LPA with $n_0 \simeq 10^{18}$ cm^{-3} produces ~ 1 GeV beams [5]. A meter-scale LPA with $n_0 \simeq 10^{17}$ cm^{-3} is anticipated to produce 10 GeV-class beams [1]. The rapid development and the properties of LPAs make them interesting candidates for applications to future compact radiation sources [6, 7, 8, 9] and high-energy linear colliders [10, 11, 12].

Modeling of LPAs requires self-consistently solving Maxwell's equations, describing the behavior of the laser and the electromagnetic fields, coupled to the equations of motion for the plasma [13]. The numerical modeling, in 3D, of LPAs is a computationally challenging task. This is due to the great disparity among the length scales involved in the simulation, ranging from the micron scale of the laser wavelength (e.g., electron quivering in the laser field) to the total laser-plasma interaction length that can be up to a meter for a 10 GeV LPA stage. In general, the computational complexity of an LPA simulation scales as $\propto (L_{\text{acc}}/\lambda_0)^{4/3}$. Here we assume that the accelerator length is the pump depletion length. For instance, a conventional 3D particle-in-cell (PIC) simulation [13] of a centimeter-scale plasma requires $\sim 10^6$ CPU hours on a modern supercomputer like Edison (Cray XC30) at the National Energy Research Scientific Computing Center (NERSC). We expect that the modeling of a meter-long, 10 GeV-class LPA stage would require $\sim 10^8$ CPU hours, and so it is practically unfeasible with standard numerical tools. However, extensive numerical modeling of current and future LPAs is required since LPA physics is, in general, highly nonlinear, and so modeling plays a central role in guiding our understanding of such physics. Detailed and extensive simulation campaigns are also required when designing an LPA experiment and/or when interpreting experimental results (e.g., exploration of parameter space to understand trends in the physics, feedback between experiment and numerical modeling to optimize experimental results, etc.).

In order to make simulations of multi-GeV LPA stages readily available, a reduction of the computational complexity of the problem is required. This can be achieved, for instance, by performing simulations using reduced physics models. Reduced models allow for a significant computational speedup compared to full PIC simulations either because of dimensionality reduction (*e.g.*, 2D cylindrical or quasi-3D instead of full 3D Cartesian) or because of approximations in the description of

the physics of the system (*e.g.*, quasi-static instead of fully dynamic plasma response, fluid instead of fully kinetic, time-averaged ponderomotive approximation instead of full Lorentz force, etc.). Even if they may lack some aspects of the LPA physics (*e.g.*, a quasi-static code is unable to describe self-injection, etc.), their use has been proven to be successful in several relevant scenarios [14, 15, 16, 17, 18, 19, 20]. Performing the simulation using the boosted Lorentz frame technique [21] also results in a reduction of the computational complexity of the problem if backward propagating waves (*e.g.*, Raman backscattering) can be neglected.

The computational framework INF&RNO [22, 23, 24] developed at LBNL, is a reduced code specifically designed to efficiently model LPAs and addresses the need for extensive numerical modeling by carefully selecting the amount and type of physics to compute. The plasma can be modeled using either a PIC or a cold fluid description, and for both modalities a (full) time-explicit or a quasi-static description can be employed. Both PIC and fluid modalities are integrated in the same computational framework allowing for staged simulations (*e.g.*, PIC-mode for injection and fluid-mode for acceleration). The code works in 2D cylindrical ($r - z$) geometry (a 1D version of the code is also available) and makes use of the time-averaged ponderomotive force approximation to describe the interaction of the laser pulse with the plasma. The adoption of the cylindrical geometry allows the description of key 3D physics (laser evolution, electromagnetic field structure) at 2D computational cost. In the time-averaged ponderomotive force approximation, the equations describing the motion of the electrons in the fields due to the laser and the wake are analytically averaged over the fast laser oscillations. The averaging removes the need to model the details of electron motion at the laser wavelength scale, and this reduces the imbalance between the physical scales involved in the modeling. In fact, in this case, the plasma wavelength (or the laser pulse length) becomes the minimum physical spatial scale. The analytical averaging is possible due to the time scale separation between the (fast) laser field, characterized by the laser frequency $\omega_0 = 2\pi c/\lambda_0$, and the (slow) wakefield, characterized by the plasma frequency, ω_p. Typically, for laser-plasma parameters of interest for LPAs, we have $\omega_0/\omega_p \gg 1$. The reduction of the computational complexity provided by the time-averaged ponderomotive force approximation can be quantified in $\sim \omega_0^2/\omega_p^2$ [25, 26, 27]. Within this approximation, we have that the wakefield evolves according to Maxwell's equations (coupled to the equations for the plasma averaged over the fast laser oscillations), while the laser driver is decomposed into a fast phase component and a slow (complex) envelope, and only the evolution of the envelope is calculated [14].

In this paper, we describe the details of the INF&RNO laser-envelope solver. Compared to other implementations of the envelope solver used in other codes [25, 26, 27], the INF&RNO solver retains the full wave operator. Furthermore, by using a polar representation for the complex envelope when solving the envelope evolution equation via a finite differences scheme, the INF&RNO solver provides an accurate description of the laser pulse evolution as it approaches depletion, even at a reasonably low resolution. This and other features, such as, for instance, the adoption of independent computational grids for the laser and the plasma [24], allow INF&RNO to achieve a speedup of several orders of magnitude compared to standard full 3D PIC simulations while still retaining physical fidelity.

This paper is structured as follows. The implementation of the INF&RNO laser solver is described in Sec. 2. In Sec. 3 we illustrate the performance of the solver. Discussions and conclusions are presented in Sec. 4.

2. Implementation of the advanced laser envelope solver

The code INF&RNO works in 2D cylindrical geometry, it adopts the normalized co-moving coordinate $\zeta = k_p(z - ct)$ (where z is the longitudinal coordinate, t is the time, and k_p is the plasma skin depth corresponding to chosen reference density n_0) to describe the longitudinal degree of freedom, and $\rho = k_p r$ as the normalized transverse coordinate. The time is normalized according to $\tau = \omega_p t = k_p ct$.

The laser field is described by means of the transverse normalized vector potential defined as $a_\perp(\zeta, \rho; \tau) = eA_\perp(\zeta, \rho; \tau)/mc^2$, where $A_\perp$ is the transverse component of the vector potential of the laser (we assume linear polarization) from which the high-frequency electric and magnetic laser fields can be computed. The laser vector potential is decomposed into a fast phase and a slow envelope according to $a_\perp(\zeta, \rho; \tau) = [\hat{a}(\zeta, \rho; \tau)/2] \exp[i(k_0/k_p)\zeta] + \text{c.c.}$ (we assume that the laser pulse propagates towards the positive z direction), where the exponential term describes the fast laser oscillations, and $\hat{a}$ is the slow (complex) laser envelope. The evolution equation for the envelope is [1]

$$\left(\nabla_\perp^2 + 2i\frac{k_0}{k_p}\frac{\partial}{\partial \tau} + 2\frac{\partial^2}{\partial \zeta \partial \tau} - \frac{\partial^2}{\partial \tau^2} \right) \hat{a} = \chi \hat{a} \,, \tag{1}$$

where $k_0 = 2\pi/\lambda_0$ is the central laser wavenumber, and $\chi = n/(n_0 \gamma_{\text{plasma}})$ is the proper density [n is the local (perturbed) electron plasma density and γ_{plasma} is the relativistic factor associated with the local plasma fluid motion, including the quiver motion in the laser field]. In deriving Eq. (1) we neglected the contribution of a high-frequency scalar potential term that is generally small for LPA-relevant parameters. A discussion of the limits of validity of Eq. (1) can be found in Refs. [1] and [14]. The first term on the left hand side (l.h.s.) of Eq. (1) describes laser diffraction, in cylindrical geometry we have $\nabla_\perp^2 = \rho^{-1}\partial_\rho + \partial_\rho^2$. The second term sets the characteristic scale of envelope evolution, typically $\partial_\tau \sim 1/(k_p Z_r)$, where Z_r is the Rayleigh length ($Z_r = \pi w_0^2/\lambda_0$ for a Gaussian laser pulse with a waist w_0). For LPA-relevant parameters we have $k_p Z_r \gg 1$. The third term on the l.h.s. of Eq. (1) describes variation in the local laser group velocity and frequency as the laser propagates in the plasma. The fourth term, describing backward propagating waves, is usually neglected in most codes that use an envelope description for the laser [25, 26, 27], but it is retained in the INF&RNO solver. This term is generally small in the early stages of the laser-plasma interaction, however it becomes important at later times when the laser is depleted [28]. The term on the right hand side (r.h.s.) of Eq. (1) represents the envelope of the rapidly varying part of the plasma current density driven by the laser and describes the coupling between the plasma and the laser (i.e., self-focusing, plasma-wave guiding, etc.). In order to solve Eq. (1) we need to know the proper density χ, and this can be determined by solving the laser envelope equation together with the equations describing the plasma (either by using a full time-explicit or a quasi-static approach). Details on how the plasma equations are solved in INF&RNO are described in Refs. [22] and [24]. In this paper, for the purpose of discussing the numerical solution to Eq. (1), we will assume that χ is known at the desired location in space and time.

To perform the temporal discretization of the envelope evolution equation we introduce the discretized time $\tau_n = n\Delta_\tau$ ($n = 0, 1, \cdots$), where Δ_τ is the temporal discretization step. We use standard centered 2nd-order finite-difference schemes to represent the first and the second time derivatives of the laser envelope, namely $\partial_\tau \hat{a}|_{\tau=\tau_n} = (\hat{a}^{n+1} - \hat{a}^{n-1})/2\Delta_\tau$, and $\partial_\tau^2 \hat{a}|_{\tau=\tau_n} = (\hat{a}^{n+1} - 2\hat{a}^n + \hat{a}^{n-1})/\Delta_\tau^2$, where

$\hat{a}^l = \hat{a}(\zeta, \rho; \tau = \tau_l)$. In addition, for the $\nabla_\perp^2$ term and for the envelope amplitude on the r.h.s. of Eq. (1), we use the Crank-Nicolson method, namely $\hat{a}|_{\tau=\tau_n} \to (\hat{a}^{n+1} + \hat{a}^{n-1})/2$. The temporal discretization of Eq. (1) then reads

$$\nabla_\perp^2 \left(\frac{\hat{a}^{n+1} + \hat{a}^{n-1}}{2} \right) + 2 \left[i \frac{k_0}{k_p} + \frac{\partial}{\partial \zeta} \right] \left(\frac{\hat{a}^{n+1} - \hat{a}^{n-1}}{2\Delta_\tau} \right) - \frac{\hat{a}^{n+1} - 2\hat{a}^n + \hat{a}^{n-1}}{\Delta_\tau^2} = \chi^n \frac{\hat{a}^{n+1} + \hat{a}^{n-1}}{2}, \tag{2}$$

where $\chi^n = \chi(\zeta, \rho; \tau = \tau_n)$. By using Eq. (2), knowing $\hat{a}^n$, χ^n, and $\hat{a}^{n-1}$ we can determine $\hat{a}^{n+1}$.

To perform the spatial discretization of Eq. (2) we introduce a 2D grid of $N_\zeta \times N_\rho$ points, where N_ζ [N_ρ] is the number of grid points in the longitudinal [radial] direction. The physical domain sampled by the computational grid is identified by the coordinates $\zeta_{\min} \le \zeta \le \zeta_{\max}$ and $0 \le \rho \le \rho_{\max}$. The grid resolution is then $\Delta_\zeta = (\zeta_{\max} - \zeta_{\min})/(N_\zeta - 1)$ in the longitudinal direction and $\Delta_\rho = \rho_{\max}/(N_\rho - 1)$ in the radial direction. A generic point on the grid is identified by the two integers (j, k), with $0 \le j \le N_\zeta - 1$ and $0 \le k \le N_\rho - 1$, and the physical coordinates of the point are (ζ_j, ρ_k), with $\zeta_j = \zeta_{\min} + j\Delta_\zeta$ and $\rho_k = k\Delta_\rho$.

For the spatial discretization of the transverse Laplacian operator in cylindrical symmetry, $\nabla_\perp^2$, we use the 2nd-order accurate expression given in Ref. [13]. For any given function $f = f(\zeta, \rho; \tau)$ [in our case $f = (\hat{a}^{n-1} + \hat{a}^{n+1})/2$], defining $f_{j,k}^l = f(\zeta_j, \rho_k; \tau = \tau_l)$, and for $k \neq 0$ (i.e., $\rho > 0$), we have

$$\begin{aligned} [\nabla_\perp^2 f]_{j,k}^l &= \left[\frac{1}{\rho} \frac{\partial f}{\partial \rho} + \frac{\partial^2 f}{\partial \rho^2} \right]_{\zeta=\zeta_j, \rho=\rho_k, \tau=\tau_l} \\ &= \frac{f_{j,k+1}^l - f_{j,k-1}^l}{2k\Delta_\rho^2} + \frac{f_{j,k+1}^l - 2f_{j,k}^l + f_{j,k-1}^l}{\Delta_\rho^2} \\ &= \mathcal{L}_k^- f_{j,k-1}^l + \mathcal{L}_k^0 f_{j,k}^l + \mathcal{L}_k^+ f_{j,k+1}^l, \end{aligned} \tag{3}$$

where $[\nabla_\perp^2 f]_{j,k}^l$ is the value of the transverse Laplacian at the spatial locations identified by (j, k) for $\tau = \tau_l$, and where $\mathcal{L}_k^\pm = (1 \pm 1/2k)/\Delta_\rho^2$, and $\mathcal{L}_k^0 = -2/\Delta_\rho^2$. For $k = 0$ (i.e., on-axis), assuming f is an even function of ρ [i.e., $f(\zeta, \rho; \tau) = f(\zeta, -\rho; \tau)$, yielding $f_{j,-1}^l = f_{j,1}^l$], we have

$$[\nabla_\perp^2 f]_{j,0}^l = \left[2 \frac{\partial^2 f}{\partial \rho^2} \right]_{\zeta=\zeta_j, \rho=0, \tau=\tau_l} = \frac{4(f_{j,1}^l - f_{j,0}^l)}{\Delta_\rho^2} = \mathcal{L}_0^0 f_{j,0}^l + \mathcal{L}_0^+ f_{j,1}^l, \tag{4}$$

where $\mathcal{L}_0^0 = -4/\Delta_\rho^2$, and $\mathcal{L}_0^+ = 4/\Delta_\rho^2$ (for completeness, we also define $\mathcal{L}_0^- = 0$). We assume reflecting boundary conditions for $\rho = \rho_{\max}$, which implies imposing $\mathcal{L}_{N_\rho - 1}^+ = 0$. This is a good assumption as long as the laser is guided (confined) and remains far from the boundary. The implementation of an absorbing boundary condition is currently underway.

Discretization of the longitudinal derivative, ∂_ζ [second term in Eq. (2)], requires particular care in order to design an accurate and efficient solver. In a code based on a laser envelope model that adopts the ponderomotive approximation to describe the laser-matter interaction, there is no need, in principle, to resolve the laser wavelength, and the characteristic length of the pulse, L, is the smallest relevant scale of interest. However, during propagation in the plasma, as a consequence of laser-pulse redshifting, structures smaller than L arise in the laser envelope [27, 28, 29]. In Fig. 1 we show,

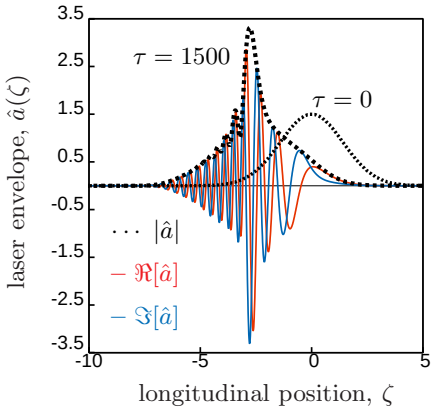

Figure 1. Evolution of the laser envelope in a 1D simulation with parameters $a_0 = 1.5, k_0/k_p = 20, L = 1$ $[a^2(\zeta, \tau = 0) = a_0^2 \exp(-\zeta^2/2L^2)]$. The dashed black lines refer to $\tau = 0$ and $\tau = 1500$. For $\tau = 1500$ the real (red) and imaginary (blue) part of $\hat{a}$ are also shown.

as an illustration, the evolution of the laser envelope from $\tau = 0$ to $\tau = 1500$ in a 1D simulation with $a_0 = 1.5, k_0/k_p = 20, L = 1$ [we assume, initially, a laser pulse of the form $a^2(\zeta, \tau = 0) = a_0^2 \exp(-\zeta^2/2L^2)$]. The red and blue lines in Fig. 1 are, respectively, the lineout of the real ($\Re[\hat{a}]$) and imaginary ($\Im[\hat{a}]$) part of the laser envelope for $\tau = 1500$. At later times during the laser-plasma interaction, the presence of structures (oscillations) in $\Re[\hat{a}]$ and $\Im[\hat{a}]$ with a characteristic length scale much smaller than the characteristic length of the envelope ($\sim L$) is evident. This has to be taken into account when designing a numerical scheme for the laser envelope evolution equation, or when choosing the longitudinal resolution to be used in the simulation. In fact, when such small-scale structures in $\hat{a}$ develop and are not well captured/resolved by the computational grid (this is the case for depleted laser pulses if the longitudinal resolution is not sufficiently high), a not optimal discrete form of the operator ∂_ζ might introduce significant numerical errors and could prevent a correct description of the laser evolution [27].

In INF&RNO this issue is addressed by means of a technique that involves the polar form for the representation of the complex field $\hat{a}$, namely $\hat{a}^{(\mathrm{p})} = a \exp(i\theta)$, where $a = |\hat{a}| = (\Re[\hat{a}]^2 + \Im[\hat{a}]^2)^{1/2}$ and $\theta = \arg(\hat{a})$, instead of the Cartesian representation, $\hat{a}^{(\mathrm{c})} = \Re[\hat{a}] + i\Im[\hat{a}]$. We found that, as a function of ζ, the polar amplitude and phase, a and θ, are reasonably well behaved and less prone to show an oscillatory behavior and/or significant variations over small scales compared to $\Re[\hat{a}]$ and $\Im[\hat{a}]$. The numerical evaluation of the longitudinal derivative of the laser envelope field using the polar form, namely $[\partial_\zeta \hat{a}]^{(p)} = \partial_\zeta a \exp(i\theta) + i\partial_\zeta \theta \hat{a}$ (instead of the Cartesian form, $[\partial_\zeta \hat{a}]^{(c)} = \partial_\zeta \Re[\hat{a}] + i\partial_\zeta \Im[\hat{a}]$), has then some numerical advantage. This is shown in Fig. (2), where we compare the real part of $\partial_\zeta \hat{a}$ computed numerically using the Cartesian (black) and the polar (red) representation of $\hat{a}$ using different longitudinal resolutions. The laser envelope $\hat{a}$ is the one presented in Fig. 1 for $\tau = 1500$. Longitudinal derivatives are computed using a 2nd-order upwind scheme, namely $\partial_\zeta f|_{\zeta=\zeta_j} = (-3f_j + 4f_{j+1} - f_{j+2})/2\Delta_\zeta$. The dashed lines refer to a case where data for $\hat{a}$ are discretized on a longitudinal grid with a resolution $\Delta_\zeta = 0.005$, high enough so that the structures (oscillations) in $\hat{a}$ are well resolved. We see that, in this

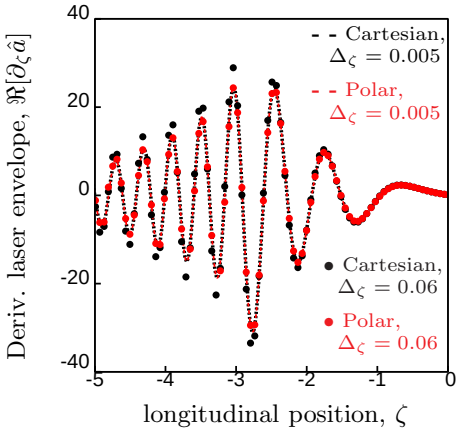

Figure 2. Real part of $\partial_\zeta \hat{a}$ computed numerically using the Cartesian (black) and the polar (red) representation of $\hat{a}$ using different longitudinal resolutions. The dashed lines refer to a case where data for $\hat{a}$ are discretized on a longitudinal grid with resolution $\Delta_\zeta = 0.005$ (high resolution case). The dots refer to a case with $\Delta_\zeta = 0.06$ (low resolution case). The laser envelope $\hat{a}$ is the one presented in Fig. 1 for $\tau = 1500$.

case, the value of the derivative obtained with both representations is essentially the same. The dots refer to a case where the envelope data are discretized on a grid with a coarse resolution ($\Delta_\zeta = 0.06$) so the structures in $\Re[\hat{a}]$ and $\Im[\hat{a}]$ are poorly resolved. We see that, even at low resolution, the value of the derivative obtained with the polar representation (red dots) is in very good agreement with that obtained in the high resolution case, while the derivative obtained with the Cartesian representation (black dots) is affected by a large error.

We notice that in Eq. (2) the operator ∂_ζ acts on $\hat{a}^{n-1}$ and $\hat{a}^{n+1}$. To simplify the algorithm (retrieving the phase is a time-consuming operation) we use the phase of $\hat{a}^n$ in evaluating both $\partial_\zeta \hat{a}^{n+1}$ and $\partial_\zeta \hat{a}^{n-1}$. Formally, the error associated with this approximation is of first order in Δ_τ. More specifically, denoting by $\theta^n = \theta(\zeta, \rho; \tau = \tau_n)$ the function describing the phase of $\hat{a}^n$, from the identity $\hat{a}^{n\pm1} = \hat{a}^{n\pm1} \exp(-i\theta^n) \exp(i\theta^n)$ we obtain

$$\frac{\partial \hat{a}^{n\pm1}}{\partial \zeta} = \frac{\partial (\hat{a}^{n\pm1} e^{-i\theta^n})}{\partial \zeta} e^{i\theta^n} + i \frac{\partial \theta^n}{\partial \zeta} \hat{a}^{n\pm1}, \tag{5}$$

where the terms $\hat{a}^{n\pm1} \exp(-i\theta^n)$ and θ^n are, respectively, approximate expressions for the amplitude and phase of $\hat{a}^{n\pm1}$ and, as shown beforehand, are smooth functions of ζ. Discretizing Eq. (5) using the 2nd-order upwind scheme for ∂_ζ gives

$$\left[\frac{\partial \hat{a}^{n\pm1}}{\partial \zeta}\right]_{\zeta=\zeta_j, \rho=\rho_k} = \frac{1}{2\Delta_\zeta} \Big[-3\hat{a}^{n\pm1}_{j,k} + 4\hat{a}^{n\pm1}_{j+1,k} e^{i(\theta^n_{j,k} - \theta^n_{j+1,k})} - \hat{a}^{n\pm1}_{j+2,k} e^{i(\theta^n_{j,k} - \theta^n_{j+2,k})} \Big] + i D^n_{j,k} \hat{a}^{n\pm1}_{j,k}, \tag{6}$$

where $D^n_{j,k} = (-3\theta^n_{j,k} + 4\theta^n_{j+1,k} - \theta^n_{j+2,k})/2\Delta_\zeta$, and where $\theta^n_{j,k} = \theta(\zeta_j, \rho_k; \tau = \tau_n)$.

We note that the choice of the upwind scheme to evaluate ∂_ζ has the advantage of allowing a simple implementation of the open boundary condition in the longitudinal direction. In fact, owing to the definition of the co-moving coordinate, for $\zeta \geq \zeta_{\max}$

(i.e., ahead of the laser driver) we can assume that all the laser-related quantities are zero. This can be easily implemented in the algorithm by adding two layers of "ghost" grid points to the right of the $\zeta = \zeta_{\max}$ boundary at a longitudinal location corresponding to $j = N_\zeta$ and $j = N_\zeta + 1$ (i.e., on the front of the computational domain), such that $\hat{a}^l_{N_\zeta,k} = \hat{a}^l_{N_\zeta+1,k} = 0$, for any k and l. On the other hand, for $\zeta = \zeta_{\min}$, the evolution of the laser envelope in the points with $j = 0$ is determined by the status of the system in the points with $j = 1$ and $j = 2$, which are within the computational domain, and no other information or condition is required.

The INF&RNO envelope solver is obtained by combining the expressions given by Eqs. (2, 3, 4, 6), we have

$$\begin{aligned}
&\frac{\mathcal{L}^-_k}{2}\hat{a}^{n+1}_{j,k-1} + \left[C^{0,+}_k - \frac{\chi^n_{j,k}}{2} + \frac{i}{\Delta_\tau}D^n_{j,k}\right]\hat{a}^{n+1}_{j,k} + \frac{\mathcal{L}^+_k}{2}\hat{a}^{n+1}_{j,k+1} = \\
&\quad - \frac{2}{\Delta^2_\tau}\hat{a}^n_{j,k} \\
&\quad - \frac{\mathcal{L}^-_k}{2}\hat{a}^{n-1}_{j,k-1} - \left[C^{0,-}_k - \frac{\chi^n_{j,k}}{2} - \frac{i}{\Delta_\tau}D^n_{j,k}\right]\hat{a}^{n-1}_{j,k} - \frac{\mathcal{L}^+_k}{2}\hat{a}^{n-1}_{j,k+1} \\
&\quad - \frac{2e^{i(\theta^n_{j,k}-\theta^n_{j+1,k})}}{\Delta_\tau\Delta_\zeta}[\hat{a}^{n+1}_{j+1,k} - \hat{a}^{n-1}_{j+1,k}] \\
&\quad + \frac{e^{i(\theta^n_{j,k}-\theta^n_{j+2,k})}}{\Delta_\tau\Delta_\zeta}[\hat{a}^{n+1}_{j+2,k} - \hat{a}^{n-1}_{j+2,k}],
\end{aligned} \tag{7}$$

where

$$C^{0,\pm}_k = \frac{\mathcal{L}^0_k}{2} \pm i\frac{k_0}{k_p}\frac{1}{\Delta_\tau} \mp \frac{3}{2}\frac{1}{\Delta_\tau\Delta_\zeta} - \frac{1}{\Delta^2_\tau}. \tag{8}$$

Once $\hat{a}^{n-1}_{j,k}$ and $\hat{a}^n_{j,k}$ are specified (initial condition), the values of $\hat{a}^{n+1}_{j,k}$ are determined by solving recursively Eq. (7) starting at the front of the computational domain ($j = N_\zeta - 1$). The solution at the longitudinal location j relies on the knowledge of the solution in $j + 1$ and $j + 2$. For any j, the values of the envelope in the N_ρ transverse points are obtained by solving a tridiagonal system. We recall that this solver, being based on a Crank-Nicolson scheme, is unconditionally stable, i.e., there is no Courant-Friedrichs-Lewy condition restricting the time step Δ_τ. The choice of Δ_τ is only dictated by the physics of the problem being modeled. We presented a derivation of the scheme in 2D Cylindrical geometry, however, extension to 2D/3D Cartesian geometry is straightforward. (In particular, in 3D Cartesian geometry the structure of the algorithm remains essentially the same as described in this paper with the tridiagonal solver replaced by a 2D Poisson solver.) A 1D version of the solver can be easily obtained from Eq. (7) taking $\mathcal{L}^\pm_k = \mathcal{L}^0_k = 0$ for $k = 0, 1, \cdots, N_\rho - 1$.

3. Performance of the INF&RNO solver

An example (in 1D) of the performance of the laser envelope solver implemented in INF&RNO is shown in Figs. 3 and 4. We consider an LPA stage with parameters $a_0 = 1$, $k_pL = 1$ [the initial laser profile is $a^2(\zeta, \tau = 0) = a_0^2 \exp(-\zeta^2/2L^2)$], and $k_0/k_p = 100$. The LPA length is $L_{\rm acc} \simeq 0.7$ m. These parameters are of interest for a 10 GeV-class LPA stage. The proper density, required to solve the laser envelope equation, was evaluated using the quasi-static 1D fluid theory [1].

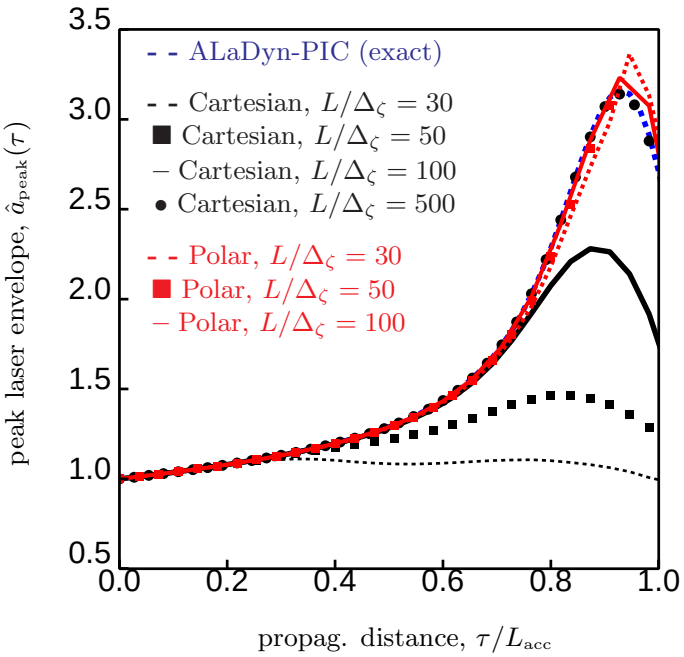

Figure 3. Evolution of the peak laser envelope as a function of the propagation distance, $\hat{a}_{\rm peak}(\tau)$, computed with different laser solvers. The laser-plasma parameters are $a_0 = 1$, $L = 1$ and $k_0/k_p = 100$. The dashed blue line is obtained with the high-order explicit PIC code ALaDyn at high resolution (40 points per laser wavelength), and can be considered exact for practical purposes. The black curves are the results obtained with an envelope solver that does not use the polar representation in evaluating the longitudinal derivatives of the laser envelope (Cartesian-based solver). The resolutions considered are $L/\Delta_\zeta = 30, 50, 100, 500$ (with $\Delta_\tau = 1$). The red curves refer to the results obtained with the INF&RNO solver Eq. (7) (polar-based solver) for $L/\Delta_\zeta = 30, 50, 100$, and $\Delta_\tau = 1$.

In Fig. 3 we plot the evolution of the peak laser envelope as a function of the propagation distance, $\hat{a}_{\rm peak}(\tau)$, computed with different laser solvers and with different spatial resolutions. The blue dashed line is the result obtained with the high-order explicit PIC code ALaDyn [30] at high resolution (40 points per laser wavelength), and can be considered exact for practical purposes (convergence verified). The black curves refer to results obtained with an envelope solver that does not use the polar representation in evaluating the longitudinal derivatives of the laser envelope (i.e., Cartesian-based solver). Different resolutions are considered, namely $L/\Delta_\zeta = 30, 50, 100, 500$, and $\Delta_\tau = 1$ (see figure for details). We see that this scheme exhibits a slow convergence rate, requiring at least a resolution $L/\Delta_\zeta \sim 500$ to obtain a correct laser evolution in the late stages of the laser-plasma interaction when the laser driver is depleted. The red curves refer to the results obtained with the INF&RNO solver Eq. (7) (i.e., polar-based solver) for $L/\Delta_\zeta = 30, 50, 100$, and $\Delta_\tau = 1$ (see figure for details). The optimized INF&RNO solver shows a much faster convergence rate compared to the previous case, and convergence is essentially reached for $L/\Delta_\zeta \sim 50$.

In Fig. 4 we plot the longitudinal lineout of the laser envelope, $|\hat{a}(\zeta)|$, for two propagation distances corresponding to $\tau/L_{acc} = 0.63$ (a) and $\tau/L_{acc} = 0.91$ (b).

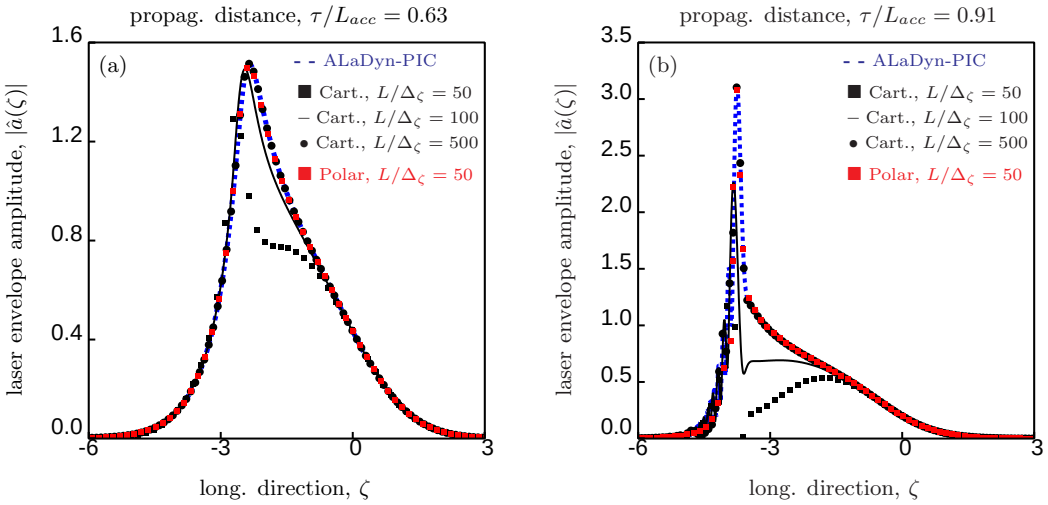

Figure 4. Longitudinal lineout of the laser envelope, $|\hat{a}(\zeta)|$, plotted for a propagation distance of $\tau/L_{acc} = 0.63$ (a) and $\tau/L_{acc} = 0.91$ (b), computed with different laser solvers. The laser-plasma parameters are $a_0 = 1$, $L = 1$ and $k_0/k_p = 100$. The dashed blue line is obtained with the high-order explicit PIC code ALaDyn at high resolution (40 points per laser wavelength). The black curves are the results obtained with a Cartesian-based solver. The resolutions considered are $L/\Delta_\zeta = 50, 100, 500$ (with $\Delta_\tau = 1$). The red curve refers to the result obtained with the INF&RNO (polar-based) solver Eq. (7) (polar-based solver) for $L/\Delta_\zeta = 50$, and $\Delta_\tau = 1$.

Different plots refer to calculations performed, as before, with different laser solvers and with different spatial resolutions. The blu dashed line is the result obtained with the PIC code ALaDyn at high resolution. The black curves refer to results obtained with a Cartesian-based envelope solver. Different resolutions are considered, namely $L/\Delta_\zeta = 50, 100, 500$, and $\Delta_\tau = 1$ (see figure for details). The red squares refer to the results obtained with the INF&RNO solver Eq. (7) for $L/\Delta_\zeta = 50$, and $\Delta_\tau = 1$. With the INF&RNO solver convergence of the laser envelope profile to the correct shape is achieved for $L/\Delta_\zeta \sim 50$, even when strongly depleted laser stages are considered, while a much higher resolution is required with a Cartesian-based solver.

The INF&RNO solver allows to obtain speed-ups of one order of magnitude compared to solvers that do not use the polar representation to evaluate the longitudinal derivatives of the laser envelope. This computational gain is obtained also in the 2D cylindrical case.

4. Discussion and conclusion

In this paper we presented the details of the accurate and efficient laser envelope solver implemented in the code INF&RNO. The solver, based on an implicit Crank-Nicolson scheme, retains the full wave operator in the envelope evolution equation, and adopts a polar representation in evaluating the longitudinal derivative of the laser envelope. We showed that the INF&RNO solver provides an accurate description of the laser pulse evolution deep into depletion, even at a reasonably low resolution, allowing for the full exploitation of the computational gains provided by the time-averaged ponderomotive

approximation. The current implementation of the envelope solver works in 1D and 2D-cylindrical geometry. Extension to 2D/3D Cartesian geometry is straightforward.

The envelope solver is a key component of the INF&RNO computational framework. The unique properties of the solver, together with other features of the code such as, for instance, the adoption of independent computational grids for the laser and the plasma, allow INF&RNO to achieve a speedup of several orders of magnitude (from 2 to 6 orders, depending on the particular problem considered) compared to standard explicit 3D PIC codes while still retaining physical fidelity. INF&RNO enables efficient and abundant modeling of multi-GeV LPAs in a reasonable time (a few hours/days) and on small computer clusters.

Acknowledgments

This work was supported by the Director, Office of Science, Office of High Energy Physics, of the U.S. DOE under Contract No. DE-AC02-05CH11231, and used the computational facilities at the National Energy Research Scientific Computing Center (NERSC).

References

[1] E. Esarey, *et al.*, Rev. Mod. Phys. **81**, 1229 (2009).
[2] S.P.D. Mangle, *et al.*, Nature **431**, p. 535 (2004).
[3] C.G.R. Geddes, *et al.*, Nature **431**, p. 538 (2004).
[4] J. Faure, *et al.*, Nature **431**, p. 541 (2004).
[5] W.P. Leemans, *et al.*, Nature Physics **2**, p. 696 (2006).
[6] W. P. Leemans, *et al.*, Phys. Rev. Lett. **91**, 074802 (2003).
[7] A. Rousse, *et al.*, Phys. Rev. Lett. **93**, 135005 (2004).
[8] M. Fuchs, *et al.*, Nature Phys. **5**, 826 (2009).
[9] A. R. Maier, *et al.*, Phys. Rev. X **2** 031019 (2012).
[10] W. P. Leemans and E. Esarey, Phys. Today **62**, 44 (2009).
[11] C. B. Schroeder, *et al.*, Phys. Rev. ST Accel. Beams **13**, 101301 (2010).
[12] K. Nakajima, *et al.*, Phys. Rev. ST Accel. Beams **14**, 091301 (2011).
[13] C. K. Birdsall, A.B. Langdon, Plasma Physics Via Computer Simulation, Adam Hilger, (1991).
[14] P. Mora, T.M. Antonsen, Phys. Plasmas **4**, p. 217 (1997).
[15] C. Huang, *et al.*, J. Comp. Phys. **217**, p. 658 (2006).
[16] I. Blumenfeld, *et al.*, Nature **445**, p. 741 (2007).
[17] A.F. Lifshitz, *et al.*, J. Comp. Phys. **228**, p. 1803 (2009).
[18] W. P. Leemans *et al.*, Phys. Rev. Lett. **113**, 245002 (2014).
[19] S. Steinke *et al.*, Nature **530**, 190 (2016).
[20] T. Mehrling *et al.*, Plasma Phys. Control. Fusion **56**, 084012 (2014).
[21] J.-L. Vay, Phys. Rev. Lett. **98**, 130405 (2007).
[22] C. Benedetti, *et al.*, AIP Conference Proceedings **1299**, 250 (2010).
[23] C. Benedetti, *et al.*, in Proceedings of PAC11 (JACoW, 2011), MOP082 (2011).
[24] C. Benedetti, *et al.*, AIP Conference Proceedings **1812**, 050005 (2017).
[25] D. Gordon, W. Mori, and T. J. Antonsen, IEEE Trans. Plasma Sci. **28/4**, 1224 (2000).
[26] Daniel F. Gordon, IEEE Trans. Plasma Sci. **35/5**, 1486 (2007).
[27] B. M. Cowan, *et al.*, J. Comp. Phys. **230** (2011) 61.
[28] W. Zhu, *et al.*, Phys. Plasmas **19**, (2012) 033105.
[29] C. B. Schroeder, *et al.*, Phys. Rev. Lett. **106**, 135002 (2011).
[30] C. Benedetti, *et al.*, IEEE-TPS **36** (2008) 1790.